Zhang *et al.*
Journal of Engineering and Applied Science (2022) 69:34
https://doi.org/10.1186/s44147-022-00085-5

Journal of Engineering and Applied Science

RESEARCH Open Access

Multi-objective optimization of heat sink with multi-cross-ribbed-fins for a motor controller

Chao Zhang[1,2*], Liang Chen[1,2] and Zhiting Tong[1,2]

*Correspondence:
czhangxj@163.com
[2] National Demonstration Center for Experimental Mechanical and Electrical Engineering Education, Tianjin University of Technology, Tianjin 300384, China
Full list of author information is available at the end of the article

Abstract

A novel multi-cross-ribbed-fin layout was proposed to supersede the original smooth fin to fulfill the lightweight requirement of the air-cooled heat sink for the electrical vehicle motor controller. The thermal design with multi-cross-ribbed-fins was optimized using the multi-objective optimization method to minimize the chip's temperature rise and the weight of the heat sink simultaneously. The design variables are the number of multi-cross-ribbed-fins ranging from 12 to 24, the number of cross ribs on either side varying from 1 to 4, and cross rib height in the region of 1.00–2.50mm. The standard k-ε turbulence model was validated compared to the experimental data for the original heat sink with smooth fins. The Pareto front solution set was obtained by performing the mixed-level orthogonal design procedure with the numerical simulations, constructing the surrogated-based model with backpropagation neural net training, and implementing the genetic algorithm. The numerical results showed that the recommended optimal designs have the multi-cross-ribbed-fin number of 17–19, the number of cross ribs of 2–3, and a cross rib height of 2.13–2.50mm. The maximum decreases in the temperature rise and weight are 7.63% and 9.45%, respectively. For verifying the superiority of current optimal designs, one of the optimal designs of the heat sink, which yields comparative temperature rise of the chip but reduced weight, was selected to be experimentally tested and compared with the data for the original heat sink.

Keywords: Heat sink, Thermal design, Multi-cross-ribbed fin, Multi-objective optimization, Pareto solution set

Introduction

As the critical component for the electric vehicle power system, the motor controller must fulfill the adequate heat dissipation capability requirements and the possible lightweight. Heat sink with proper smooth fins is a standard solution due to its higher heat transfer performance and economy [1]. In recent years, with the increasing trend of the power consumption for the motor controller, the urgent requirement of the heat dissipation capability is critically essential.

Many research works have been devoted to enhancing the heat dissipation capability of the heat sink, which can be mainly summarized as the following four aspects.

The first kind of method is replacing the long flat-plate fins with short ones. The short flat-plate fin configuration is supposed to interrupt the boundary layer and generate additional secondary flow vortexes, resulting in heat transfer improvements, especially for the staggered layouts [2, 3]. Feng et al. [4] proposed the cross-finned heat sink configuration and found a gain of 11% on the overall heat transfer coefficient relative to the traditional parallel-plat fin configuration. Zhang et al. [5] proposed the W-type finned heat sink with inclined fins. Their experimental results showed that the metal baseboard shows a temperature reduction of 4.9 °C with a decrease in the overall heat transfer area by 10% simultaneously. The heat transfer and flow characteristics of the sinusoidal wavy plate-fin heat sink were investigated by Nilpueng et al. [6]. They found that the truncation of the sinusoidal wavy plate-fin results in a 5.9–19.1% enhancement on the heat transfer performance, and a phase shift of 180° has the highest thermal performance factor. The second category is some modifications around the baseboard between the adjacent channels. Zhou and Catton [7] numerically compared the thermal-hydraulic performances of several pin-fin configurations with various cross-sections, e.g., circular, square, and elliptic. They found that the square pin-fins give the best heat transfer and the largest power consumption. The achievements in the compact plate-pin fin heat sinks can be referred to in the literature review by Al-damook and Alkasmoul [8]. The pyramidal ribs were applied by Ahmed [9] over the bottom surface between the channels for a plate-fin heat sink to improve the heat removal. The plate-fin heat sinks with fillet profiles were proposed by Wong and Indran [10], Hussain et al. [11], and Freegah et al. [12] to enhance the thermal performance by 13–31.6%, as compared with the original plate-fin heat sink. This method could directly and effectively remove heat from the metal baseboard but increase manufacturing costs, especially in the narrow space between two adjacent fins. The third kind of method is modifying the flat fin self to increase its heat transfer capability. Singh and Patil [13] inserted the semi-cylindrical impressions on the fin surface to induce the augmented flow of the boundary layer. Their experimental data found that the embossed impressions exhibit a maximum augmentation in the Nusselt number of 2.86 times relative to the smooth fin. Gupta et al. [14] studied the heat transfer enhancement for the plate-fin heat sink induced by the additional dimples and protrusions and provided the suggested dimple geometry and layout with maximum fin performance. Tariq et al. [15] validated the superiority of the multiple perforations and slots in a plate-fin heat sink using the conjugate heat transfer model and complementary experimentation. The increments of 35.9–42.8% on heat transfer performance and the weight reductions were found for their novel flat-fin heat sink because of slots and perforations. In recent research, Khudhur et al. [16] compared the heat transfer performance with different fin geometry in a flat plate-fin heat sink. They found that the flat with adding semicircular fin and the flat with subtracting semicircular fin result in heat transfer enhancement of 21% and 32% compared to the flat plate fin.

On the other hand, a proper combination of geometry parameters can benefit the thermal design for a specified finned heat sink. Li and Chen [17] studied the effect of the fin width and height on the cooling performance of the plate-fin heat sinks under confined impinging jet conditions and recommended the corresponding optimal values.

Osorio et al. [18] correlated the heat transfer performance as a function of shape, width, and area of thin flat-plate fins and obtained the optimal geometrical parameters with maximum heat transfer coefficient.

As the heat transfer performance increases, the pumping power consumption or the weight of the heat sink typically increases during the optimization processes [19, 20]. Several indexes, such as the performance evaluation criteria [21] and JF factor [22], were provided to evaluate the comprehensive performance of the heat transfer and the pumping power. Unlike a single evaluation index, a more fundamental way is to perform the multi-objective optimization [23–25] to balance the heat transfer enhancement and pumping power increase. Because of the high cost of the numerous experimental works, computational fluid dynamics (CFD) simulation has been proven as a promising and low-cost way using the validated numerical method. Elasyed and Lacor [26] pointed out that the artificial neural network (ANN) algorithm better describes the nonlinear relationship between the optimal target and independent design parameters than the RSM method with explicit expression. Various advanced optimization methods, for instance, response surface method (RSM), teaching-learning-based optimization [27], particle swarm optimization algorithm [28, 29], and genetic algorithm (GA) [30], were adopted to facilitate the multi-objective optimal design of the heat sink with many variables. Although various metaheuristic optimization algorithms were successfully applied for the heat sink optimization, the combination of ANN and Non-dominated Sorting Genetic Algorithm II (NSGA-II) is a mature and feasible way for the multi-objective optimization problem with multivariate, as proven by several relevant studies [31–34].

The literature review shows that the multi-objective optimization targets are commonly the maximum heat transfer performance and minimum pumping power consumption or pressure loss, and the reduction of heat sink weight is not considered. In the present study, the heat sink is applied to dissipate the heat load from the motor controller for the electrical drive truck. The pumping power consumption is not considered an evaluation index, as there is no fan to blow the air across the smooth fins. Hence, the trade-off between the heat transfer performance and the weight is performed to find the optimal design of the heat sink, which is different from the traditional optimization target. A novel multi-cross-ribbed-fin (MCRF) configuration was presented to replace the original smooth fin configuration to decrease the temperature rise of the chip and the weight of the heat sink simultaneously. The multi-objective optimization work was finally accomplished using the NSGA-II genetic algorithm with a combination of CFD simulations for generating sampling data, a backpropagation (BP) neural network method for constructing a surrogated model.

Methods

The general methodology flow chart is shown in Fig. 1 to present the investigated work in the current paper. Firstly, the benchmark experimental measurement for the original heat sink with smooth flat plate-fins was carried out to provide the data to validate the numerical method. Then, a set of sampling data for the novel MCRF heat sinks was obtained by performing the experiment design coupled with the CFD simulations. The surrogate model, describing the nonlinear relationship of the objective function to the design variables, was gained with BP training. Next, the GA multi-objective optimization

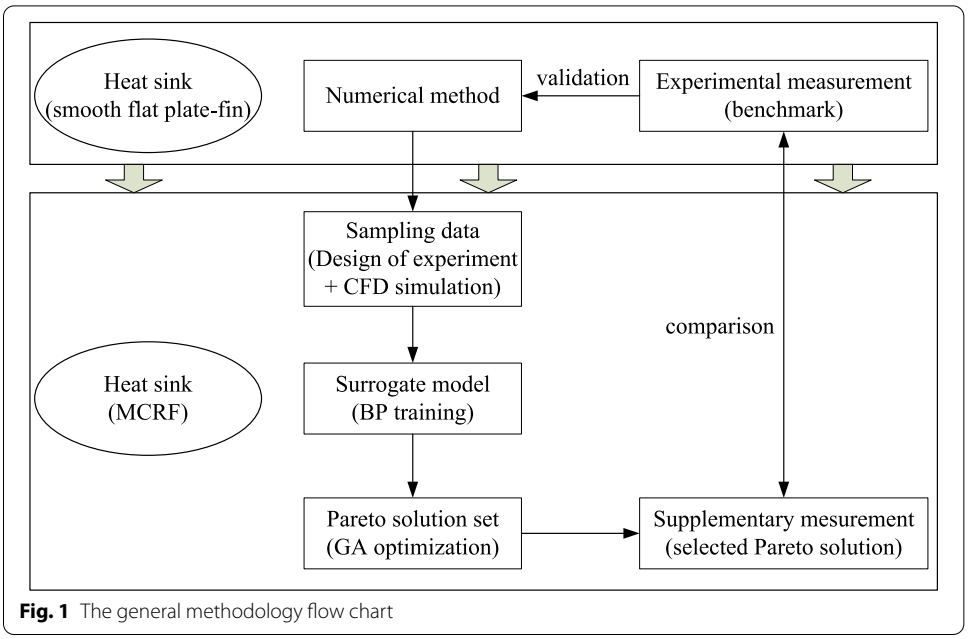

Fig. 1 The general methodology flow chart

was performed to achieve the Pareto solution set. Finally, one of the Pareto solutions was selected to verify the superiority of the current methodology, and a supplementary experiment for the optimized MCRF heat sink was tested compared to the original heat sink.

Problem statement

The original design sketch of the heat sink for the motor controller is shown in Fig. 2. In practice, the fin is usually wedge-shaped based on the cold rolling technology for low-cost manufacturing. The heat sink has a streamwise length of 220 mm and a total width of 180 mm. The heat sink material is aluminum alloy 6063 with a high heat conductivity. The baseboard has a thickness of 3.5 mm, and the height of the fin is 18.5 mm. There are 28 parallel smooth fins located on the baseboard with a pitch of 5.5 mm. The thicknesses of the fin at the tip and the root are 0.9 mm and 1.5, respectively. The total weight of the heat sink with fins and the baseboard is 0.742 kg. The orientation of the smooth fin is identical to the direction of flowing air.

A novel MCRF configuration with higher heat dissipation potential was proposed to replace the smooth fin and thus reduce the number of MCRFs. The modification of the MCRF is to add several cross-ribs on either side of the parallel fin, shown in Fig. 3. The interval of cross-ribs is 4.0 mm, and the distance between the fin tip and the center of the cross-rib is 1.0 mm. The cross-rib has a width with a constant value of 1.0 mm. The stagger arrangement of the cross-ribs is assigned with an interval of 2.25 mm. The height of the cross-ribs is also given with the same value h. Symbols N_c and N_f designate numbers of the cross-ribs on one side of the MCRF and MCRFs for the heat sink, respectively.

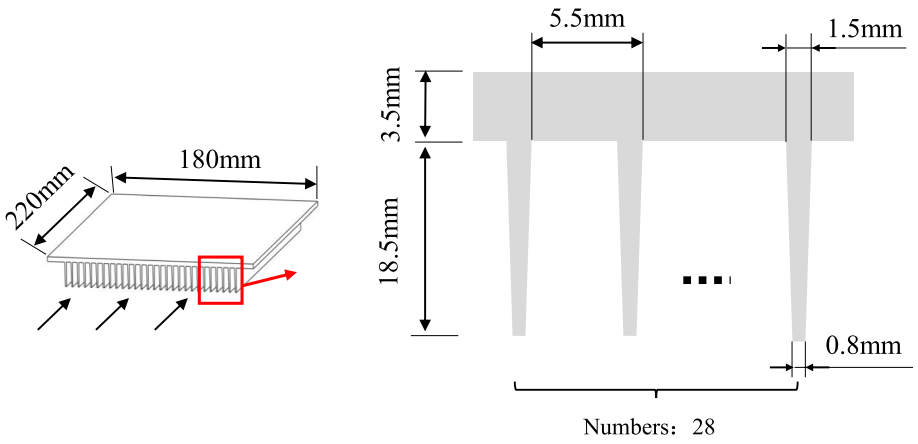

Fig. 2 The layout of the original heat sink with smooth fins

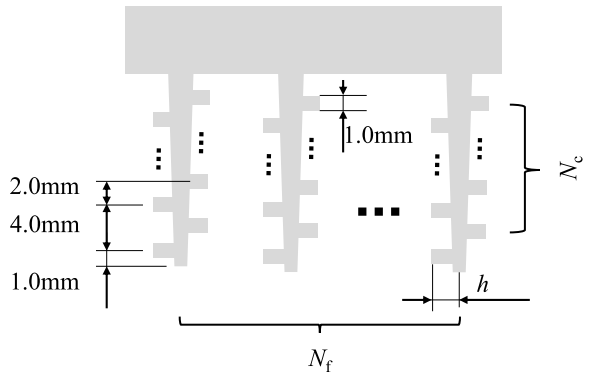

Fig. 3 Cross view of the modified heat sink with MCRFs

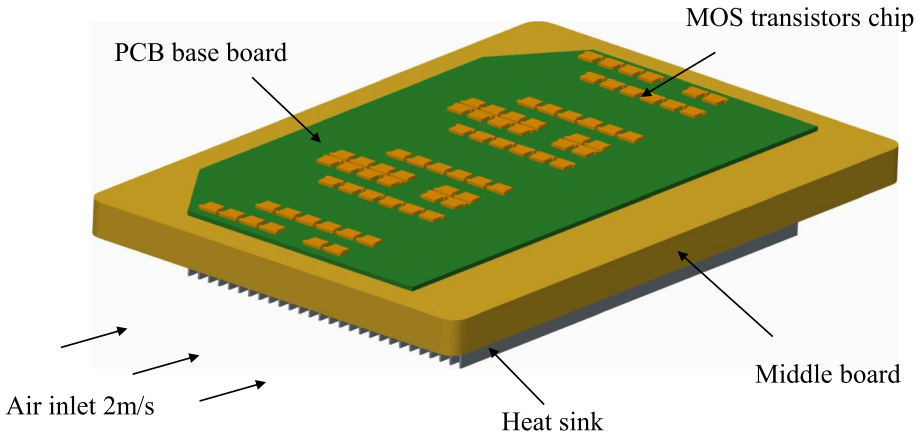

Fig. 4 Overview of the motor controller

Boundary condition and numerical method

Due to the complex composition of the air-cooled motor controller, the physical model should be simplified in advance for present simulations, which is illustrated in Fig. 4. The metal-oxide-semiconductor (MOS) transistors chips are welded with the printed circuit board (PCB) baseboard with aluminum material. The PCB baseboard is mounted on one side of the middle aluminum board, and the heat sink baseboard is mounted on the other side of the middle aluminum board. The ambient air with a velocity of 2 m/s flows to the heat sink to remove the heat load.

Because of the incomplete coincidence of the adjacent surfaces, the contact thermal resistance is set in each contact conduction surface with a value of 0.001 (m^2·K)/W. The analysis of the heat generation for the motor controller shows that the heat mainly comes from the conduction loss and the MOS transistors chip. The thermal power consumption of each MOS transistor chip is 10.52W. Thus, the boundary condition of constant heat flux of 22286W/m^2 is set on the top surface of the MOS transistors chip. The other surfaces of the PCB base board, the top surface, and the middle board's side surfaces are all assumed to be the non-slip heat insulation surfaces. The bottom surface of the middle board and all the surfaces of the heat sink are fluid-solid interfaces.

The steady-state, three-dimensional conjugate heat transfer and flow are solved in the present study using the commercial software ANSYS CFX. In the solid domain, the Laplace equation is considered to investigate heat conduction, given as follows:

$$\nabla \cdot (k_s \nabla T) = 0 \tag{1}$$

where k_s is the heat conductivity of the solid material and T is the solid temperature.

The time-averaged Navier-Stokes equations are solved in the fluid domain to investigate the convective heat transfer. The relevant mass, momentum, and energy conservation equations are provided as follows:

$$\nabla \cdot (\rho \mathbf{U}) = 0 \tag{2}$$

$$\nabla \cdot (\rho \mathbf{U} \otimes \mathbf{U}) = -\nabla p + \nabla \cdot \tau \tag{3}$$

$$\nabla \cdot (\rho \mathbf{U} h) = \nabla \cdot (k_f \nabla T) + \mathbf{U} \cdot \nabla p + \tau : \nabla \mathbf{U} \tag{4}$$

where ρ is the density, $\boldsymbol{U}$ is the velocity vector, p is the static pressure, h is the static enthalpy, k_f is the heat conductivity of the fluid, τ:$\nabla \mathbf{U}$ is the viscous dissipation, and τ is the stress tensor defined as follows:

$$\tau = \mu \left[\nabla \mathbf{U} + (\nabla \mathbf{U})^T - \frac{2}{3} \delta (\nabla \cdot \mathbf{U}) \right] \tag{5}$$

where μ is the dynamic viscosity.

At the fluid-solid interfaces, conversations of temperature and heat flux are guaranteed. For the turbulence model, the universal two-equation turbulence model, i.e., the standard k-ε model, is adopted in the present study due to its robustness and enough accuracy in the prediction of heat transfer of the heat sink. The details of the standard k-ε model can be referred to in the theory guide of ANSYS CFX software. A

second-precision scheme discretizes all the terms in governing equations. The thermal energy equation is selected for the heat transfer model due to the low velocity of airflow. When the normalized residual of each variable is less than 1.0×10^{-5}, the CFD simulation is convergent.

The unstructured grids are generated using a package ICEM CFD in solid and fluid domains. The grid nodes in the fluid and solid sides at the fluid-solid interface are one-to-one matched. The grid independence test was performed in advance to get trusted results from the CFD simulations. When the predicted values of the temperature rise of the chip in relative to ambient temperature ΔT has little change between the current grid and the finer grid, the grid independence test is completed. Table 1 lists prediction results of ΔT for the original heat sink with five sets of computational grids. The grid level varies from 0.85 to 21.96 million according to the change of global size from 0.85 to 0.40mm. As the global grid size decreases from 0.85mm (grid 1) to 0.5mm (grid 4), the grid level increases from 4.38 to 14.91 million, and the temperature rise of the chip reduces from 38.15 to 37.35K. If further increasing the grid level, the value of ΔT keeps almost unchanged. Consequently, grid 4 is adopted for the CFD simulations for the original heat sink. Following a similar way, the grid independence tests are further implemented for the heat sink with MCRFs, and the corresponding grid numbers range from 5.17 million to 18.68 million according to specific MCRFs.

Experimental facility and test procedure

The experimental measurement is operated on a specially designed electric vehicle test platform to simulate the motor controller prototype's rated and part-load operating conditions. This test platform mainly consists of a direct current (DC) power supply, a permanent magnet synchronous motor, a motor controller with heat sink, a monitoring computer, and a power measuring system including an electric power dynamometer motor, a frequency converter, a dynamometer, and a power analyzer. The schematic diagram of this test platform is shown in Fig. 5.

The DC power supply with nominal voltage 144V and nominal current 180A is used to provide the DC currents of the motor controller and the dynamometer frequency converter. Various operating conditions for the electric vehicle are simulated by changing the working conditions of the permanent magnet synchronous motor through the motor controller. By adjusting the output current and voltage from the DC power supply, the rated working condition of the motor controller can be obtained. Due to the current

Table 1 The temperature rises of the chip with different levels of computational grids

Grid	Grid size	Grid level	The temperature rise of the chip ΔT (K)
grid 1	0.85mm	4.38 million	38.14
grid 2	0.75mm	5.81 million	37.61
grid 3	0.6mm	9.94 million	37.72
grid 4	0.5mm	14.91 million	37.35
grid 5	0.4mm	21.96 million	37.32

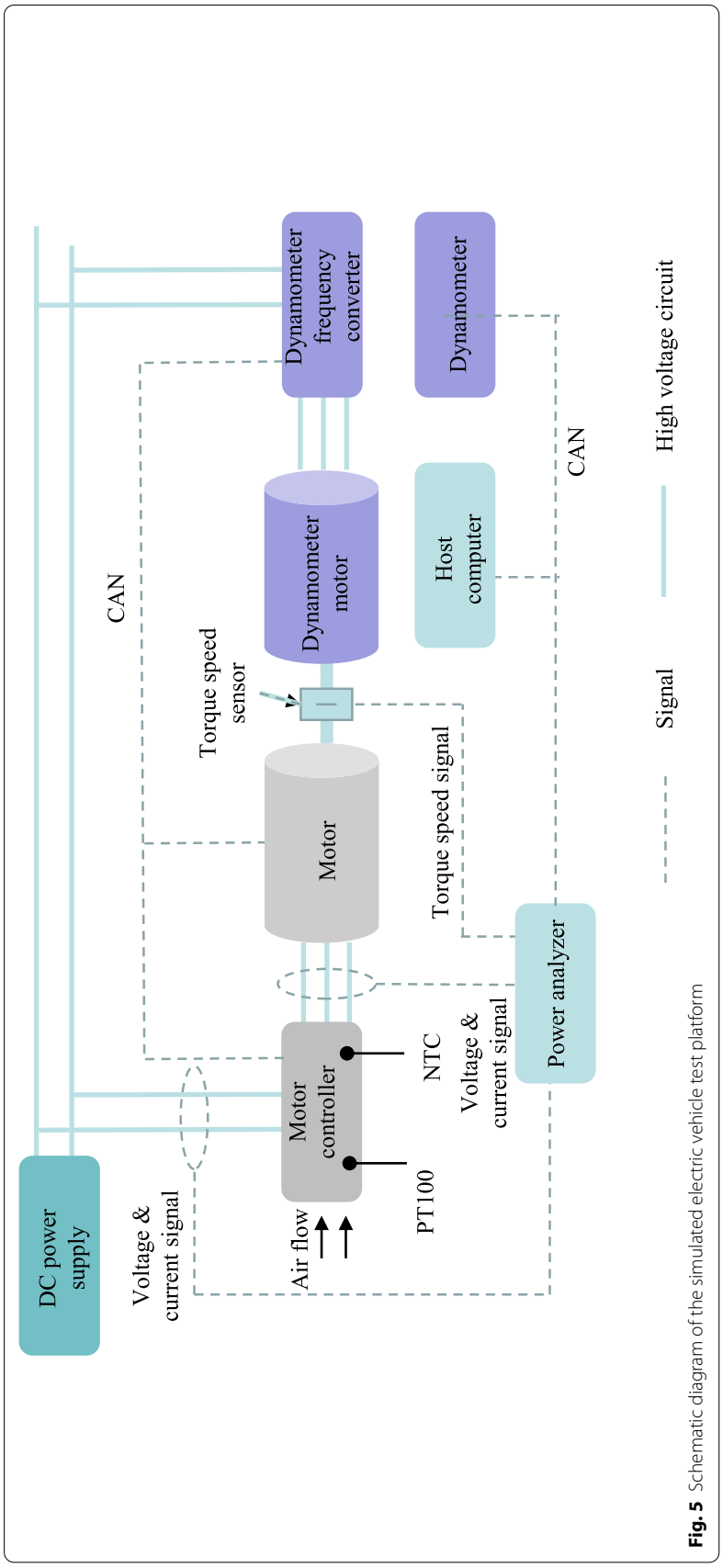

Fig. 5 Schematic diagram of the simulated electric vehicle test platform

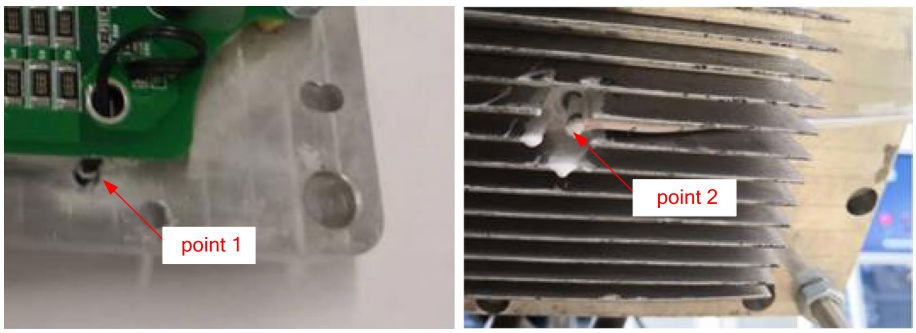

Fig. 6 Mounting positions of the temperature measurements

Table 2 Variation ranges of independent variables

Symbol	Lower value	Upper value
Number of MCRFs, N_f	12	24
Number of cross-ribs on one side of the MCRF, N_c	1	4
Cross-rib height, h (mm)	1.0	2.5

measurement focus on the heat transfer performance of the heat sink, the measurement procedure and facilities relating to the heat sink are introduced in detail. An electric fan provides the air flowing through the heat sink. The blade type anemograph with an accuracy of 3% is used to measure airflow velocity. Due to the MOS transistor's chips working with high voltages and having relatively small volumes, the chip's temperature cannot be directly measured. In the present study, two measurement points are arranged inside the baseboard of the heat sink in the current experiments, which can be seen in Fig. 6. A negative temperature coefficient thermistor thermometer is used to measure the temperature at point 1 with an accuracy of 1%. A PT100 thermometer with an accuracy of 0.1 °C is to measure the temperature at point 2.

Two designs of the heat sink, i.e., the original design with smooth fins and an optimized design with MCRFs, are tested both at the rated working conditions of the motor controller. First, the original heat sink is tested to supply the baseline data for comparison and numerical method validation. The experimental data for an optimized design is then obtained to validate the superiority of present multi-objective optimization. Due to no additional heating equipment being adopted in the current test platform, the temperature of the flowing air to cool the motor control is equal to the ambient temperature. This difference between the ambient temperature at the experimental condition and the working temperature for optimization will result in some difficulty, which will be discussed in the following section.

Optimal design framework

The independent design variables of the heat sink with MCRFs are N_f, N_c, and h. According to practice considerations on the heat sink, the variation ranges of the three design variables are listed in Table 2. The optimized objectives are minimizing the temperature

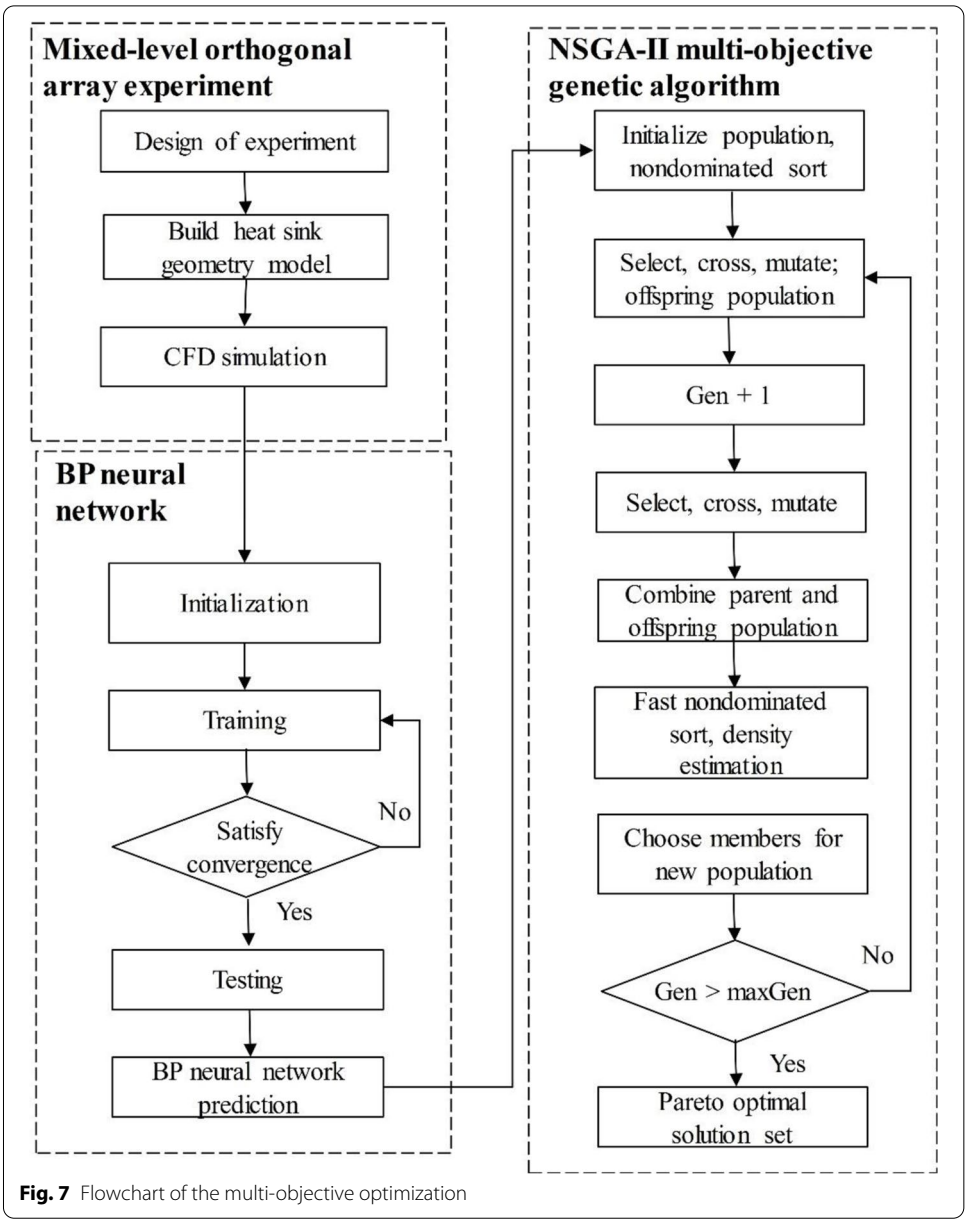

Fig. 7 Flowchart of the multi-objective optimization

rise of the chip and minimizing the weight of the heat sink, which are respectively considered for the heat transfer capability and the weight reduction. If the three design variables are given with different values, the temperature rise of the chip and the heat sink weight are changed accordingly. For the heat sink of the motor controller, these two objectives are commonly conflicted. Present multi-objective optimization work aims to find the designs at which both goals are at acceptable optimal solutions.

The flowchart of the multi-objective optimization for the heat sink with MCRFs is given in Fig. 7. The optimization process comprises three sequential sections, i.e., generating design samples using the mixed-level orthogonal array experiment, constructing a surrogated-based model using the BP neural network, and gaining the Pareto solution set using the NASA-II genetic algorithm. An in-house code is developed

based on the relevant built-in functions in software Matlab to perform the BP neural network training and genetic algorithm.

For an optimization problem, enough and effective design samples are crucial to modeling the functions between the objectives and the design variables. In the present study, the sampling results of the two evaluation indexes are all obtained by performing the CFD simulations with different values of design variables. The mixed-level orthogonal array experiment is designed to get the representative design points according to the constraint range of the design variables. Note that the values of the design variables are uniformly dispersed, flat, and neat to obtain typical results with as few tests as possible. Based on the variation ranges, the design variables' levels are 7 for N_f, 4 for both N_c and h. Thus, a mixed-level orthogonal array $L_{28}(7\times4^2)$ is formed, listed in Table 3. Note that the values of design variables N_f and N_c must be both integers.

The BP neural network is widely applied to describe the strong nonlinearity relationship for multi-input multi-output systems [35], exhibiting a feedforward multilayer neural network with the constant approximation of expected output. Based on the results from the samples, the BP neural network is initialized to determine the input and output parameter values. Then, according to the prediction error of the data, the network values and thresholds are modified continuously. The neural network is trained until the prediction results approach the expected error value. A three-layer structure is used to investigate the present BP neural network, including the input, hidden, and output layers. The input parameters of the input layer are the three design variables, and the output parameters of the output layer are the temperature rise of the chip and the heat sink weight. For the current BP neural network, the neurons number in the hidden layer is set to 10, the target threshold of the mean square error is 10^{-4}, and the maximum training number is 5000. The current BP neural network training performance for the sampling points is presented in Fig. 8. The regression line of the output relevant to the target of the trained BP neural network showed a strong linear relationship. The correlation

Table 3 The mixed-level orthogonal array for CFD simulations

Design No.	N_f	N_c	h(mm)	Design No.	N_f	N_c	h(mm)
1	24	1	1.0	15	18	3	1.5
2	24	2	1.5	16	18	4	1.0
3	24	3	2.0	17	16	1	1.0
4	24	4	2.5	18	16	2	1.5
5	22	1	1.5	19	16	3	2.0
6	22	2	1.0	20	16	4	2.5
7	22	3	2.5	21	14	1	1.5
8	22	4	2.0	22	14	2	1.0
9	20	1	2.0	23	14	3	2.5
10	20	2	2.5	24	14	4	2.0
11	20	3	1.0	25	12	1	2.0
12	20	4	1.5	26	12	2	2.5
13	18	1	2.5	27	12	3	1.0
14	18	2	2.0	28	12	4	1.5

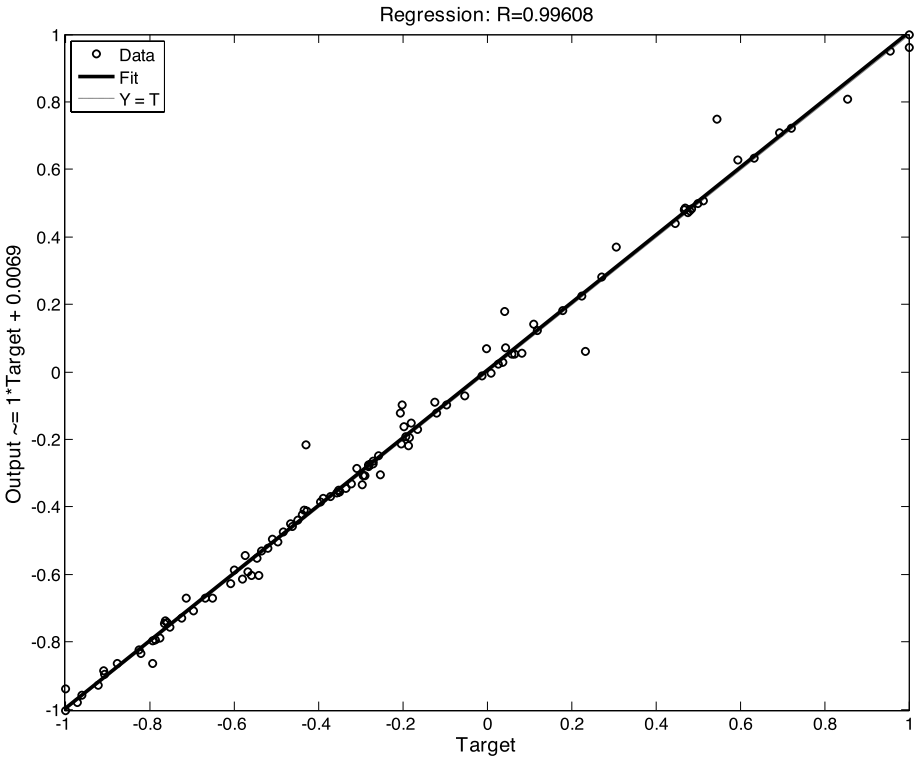

Fig. 8 Flowchart of the multi-objective optimization

Table 4 Comparison of temperature rise between CFD results and experimental data

	Experimental data ΔT (K)	ΔT_{CFD} (K)	ΔT_{error} (%)
Measurement point 1	34.93	33.79	−3.26%
Measurement point 2	34.20	33.52	−1.96%

coefficients of training, testing, and total samples were 0.99812, 0.99440, and 0.99608, respectively.

The NSGA-II algorithm [36] is a non-dominated multi-objective optimization algorithm with an elite retention strategy, which is feasible and appropriate to specify the optimal solution. For the current NSGA-II algorithm, 50% of the samples are generated randomly as the initial population. The fitness function modeled using the BP neural network previously of the intimal population is evaluated, and individuals with high fitness are genetically manipulated. The individual participating in the selection, mutation, and crossover are combined into a new generation until the convergence stop condition is satisfied. Finally, the individual with the best fitness in the offspring will be the optimization results of the genetic algorithm to gain the Pareto optimal solution set.

Results and discussion

CFD method validation

Before performing the CFD simulations, the present numerical model is validated with reliable experimental data. Therefore, the original heat sink experiment is conducted to

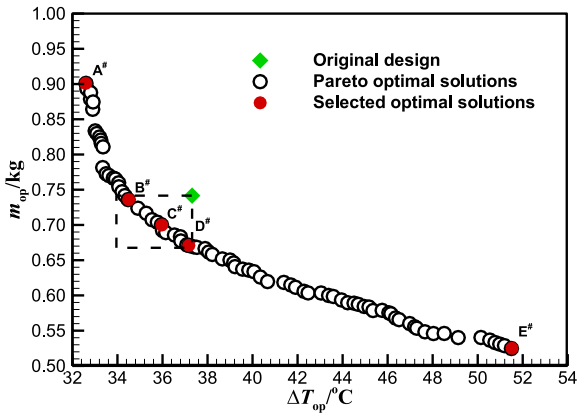

Fig. 9 Pareto optimal solution set and selected optimal solutions

Table 5 Validation of the optimization results

Design	N_f	N_c	h(mm)	ΔT_{op}(°C)	ΔT_{CFD}(°C)	ΔT_{error}(%)	m_{op}(kg)	m(kg)	m_{error}(%)
A#	24	4	2.50	32.59	32.95	−1.09	0.901	0.903	−0.22
B#	18	3	2.50	34.50	34.78	−0.81	0.736	0.735	0.14
C#	19	2	2.22	35.97	36.36	1.07	0.700	0.701	−0.14
D#	17	2	2.43	37.17	37.43	−0.69	0.671	0.672	−0.15
E#	12	1	1.00	51.52	50.80	−1.42	0.525	0.539	−2.60

get the temperatures at the two measurement points. The ambient temperature of the bench experiment is 32 °C, which is inconsistent with the maximum working environment. Hence, the temperature rise relative to the ambient temperature is taken for the evaluation target to minimize the influence of the ambient temperature. Table 4 lists predicted temperatures on the same locations as those of the experiment are compared with the experimental data. The testing and CFD predicted temperatures at point 1 are higher than those at point 2. The relative errors at measurement points 1 and 2 are −3.26% and −1.96%, respectively, within the error range in practical engineering applications. Therefore, the comparison in Table 1 demonstrates the reliability of the CFD results with the current numerical method and boundary conditions.

Pareto optimal solutions

The Pareto optimal solutions for the heat sink with MCRFs are shown in Fig. 9, which depicts the conflicted relationship between the temperature rise of the chip ΔT_{op} and the weight of the heat sink m_{op}. The variation of the design variables leads to the opposite changing trend for the two objectives. Designers can select a proper design along the curve of the Pareto optimal solution set according to the specific requirement and preference for the heat sink.

Five designs labeled design A# to E# covering the whole region of the curve in Fig. 8 are selected to validate the prediction accuracy of current multi-objective optimization work. Design A# has the minimum temperature rise of the chip but the maximum weight among possible optimal designs. On the contrary, design E# exhibits the

maximum temperature rise of the chip but the minimum weight. Design B#, C#, and D# have a moderate temperature rise of the chip and the weight in the meantime. Three-dimensional computational models of the heat sink with specific design variables for the five selected design points are constructed and simulated using the CFD method. The predicted results of design A# to design E# are compared with the values obtained from the CFD simulations, listed in Table 5. The subscript p, m, and error variables denote the values obtained from the optimization prediction, model simulation, and relative error. As shown in Table 5, the relative errors are all quite small, with the maximum value of −1.42% and −2.60% for the temperature rise of the chip and the heat sink weight of design E#. The small relative errors indicate that the current multi-objective optimization works well with acceptable accuracy.

The heat sink with MCRFs aims to replace the layout with smooth fins with higher heat transfer performance and lighter weight. Hence, the plans with a lower temperature rise of the chip and lighter weight deserve more attention. The heat transfer coefficient distributions on the side surfaces of the smooth fin for the original heat sink and the MCRFs for the optimized heat sinks are shown in Fig. 10. The heat transfer performance is augmented by imposing additional cross-ribs on the smooth surface for optimal design, especially over the section around the cross-ribs. Moreover, the improvement in the heat transfer coefficient increases with more cross-ribs. Thus, a single MCRF for design B# exhibits the best heat transfer performance among these three optimal designs.

The contours of the temperature rise of the chip on the top surfaces of the MOS transistors chip under top-view are further shown in Fig. 11 for the original design and designs B#, C#, and D#. The cooling capability of the airflow successively reduces following the flowing air. Therefore, the downstream of the chips has lower temperature rises than the upstream chips. This phenomenon occurs for neither the original design nor the optimal design. It can be seen that the temperature rise of the chips for design B# is the lowest, while the temperature rises of the chips for the original design and the design D# are almost the same. Despite fewer MCRFs for the heat sink, design B# performs the lowest temperature rise of the chip due to its best heat transfer performance of individual MCRF. Design D# shows the almost identical distribution of the temperature rise of the chip as the original design but has fewer MCRFs and thus lighter weight.

As can be seen from Fig. 9, there are 13 Pareto optimal solutions located on the lower-left corner of the original design between design B# to design D#, which are the suggested designs with improvements on both objective functions. The designer can choose any design among them based on practical requirements. The corresponding design variables and the improvement of objective functions for the suggested optimal designs are listed in Table 6. Variables ΔT_{sub} and m_{sub} denote the relative reductions of the temperature rise of the chip and the heat sink weight for the optimal designs as compared with those for the original design. The optimal design 1# gains the maximum ΔT_{sub} with a value of 7.63%, but the minimum m_{sub} with a discount of only 0.67% of the heat sink weight. The optimal design 13# has the maximum m_{sub} with a value of 9.45% but the minimum ΔT_{sub} with a value of 0.48%. Other suggested optimal designs yield moderate thermal performance and weight performance. The optimal design variables can be recommended as follows, the number of the MCRFs N_{f} ranging from 17 to 19, the number of cross-ribs on one side of MCRF N_{c} varying 2 or 3, and the height of the cross-ribs h

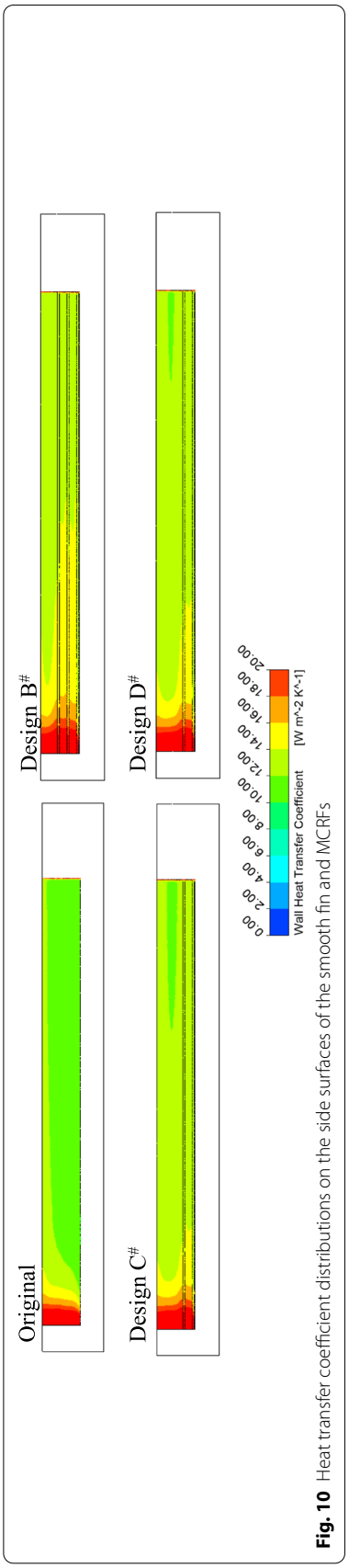

Fig. 10 Heat transfer coefficient distributions on the side surfaces of the smooth fin and MCRFs

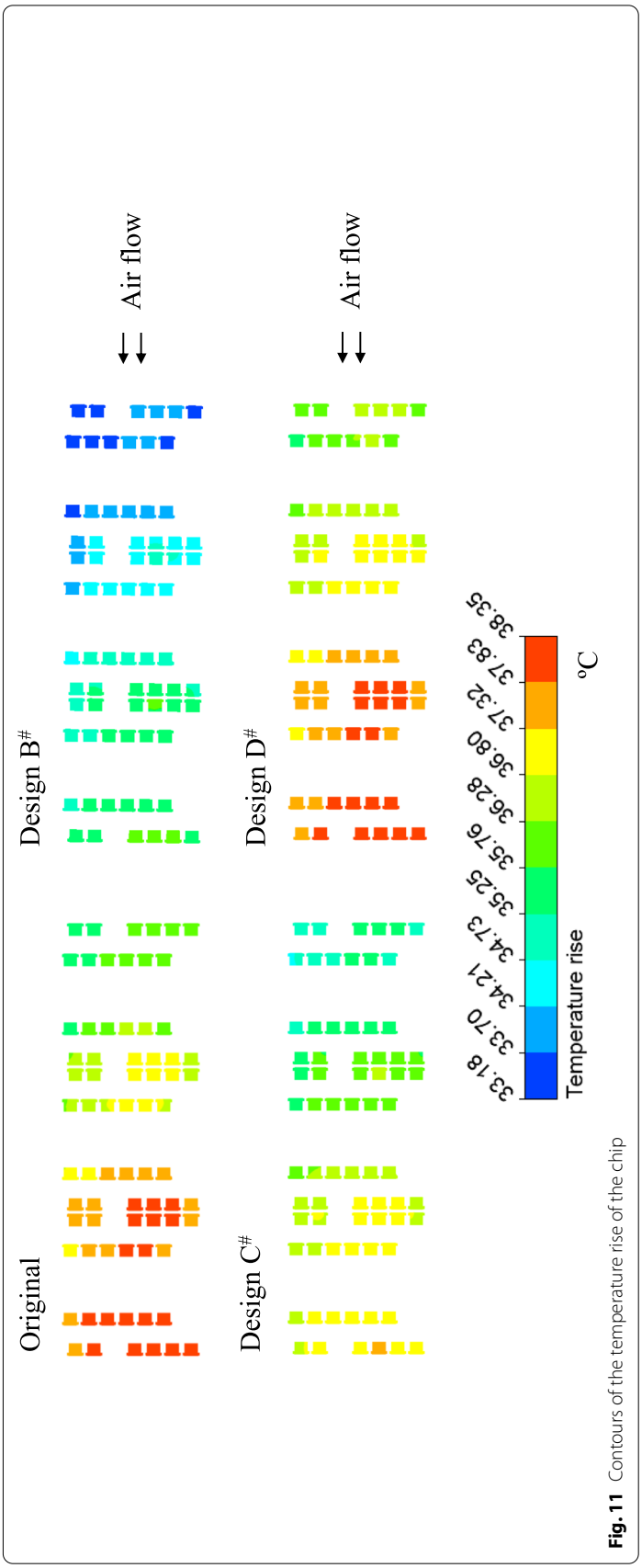

Fig. 11 Contours of the temperature rise of the chip

Table 6 The suggested optimal solution set

Design	N_f	N_c	h(mm)	ΔT_{sub}(%)	m_{sub}(%)
Original design	28	-	-	0.00	0.00
Optimal 1# (design B#)	18	3	2.50	7.63	0.67
Optimal 2#	18	3	2.22	6.48	2.29
Optimal 3#	18	3	2.13	5.60	3.38
Optimal 4#	19	2	2.41	4.87	4.59
Optimal 5#	19	2	2.28	4.20	5.13
Optimal 6# (design C#)	19	2	2.22	3.70	5.53
Optimal 7#	18	2	2.50	3.70	6.61
Optimal 8#	18	2	2.44	3.16	7.15
Optimal 9#	18	2	2.32	2.20	7.56
Optimal 10#	18	2	2.23	1.45	7.83
Optimal 11#	17	2	2.50	1.39	8.77
Optimal 12#	17	2	2.45	0.75	9.31
Optimal 13# (design D#)	17	2	2.43	0.48	9.45

ranging from 2.13 to 2.50mm, which process the practical significance for designing the heat sink with MCRFs.

Experimental test for the optimal design

To further describe the improved thermal performance of optimal design for the heat sink with MCRFs, a suggested optimal design labeled as design 11# is selected to perform the experimental test. The experimental conditions are the same as those for the original design, except for the different heat sinks. The reassembled motor controller and the details of heat sink design 11# are shown in Fig. 12.

Moreover, one of the objective functions, i.e., the temperature rise of the chip, is optimized with the maximum ambient temperature of 55 °C for the heat sink. Due to the temperature of the flowing air depending on the ambient temperature only, the optimal design experiment is operated under a different ambient temperature of 18 °C with the original heat sink. The temperature rises of measurement points 1 and 2 for the optimal design are 33.68 °C and 33.30 °C, respectively. The different ambient temperature brings difficulty to explain the superiority of the optimal design 11# using current experimental data. Considering the validated accuracy of the present numerical model, additional CFD simulations with two experiment ambient temperatures are carried out to overcome this problem.

The temperature rises of the chip and at the measurement points 1 and 2 obtained from CFD simulations at ambient temperatures of 18 °C, 32 °C, and 55 °C are shown in Fig. 13 for both the original heat sink and the optimal design 11#. At either ambient temperature, the optimal design 11# always has slightly lower temperature rises of the chip and two measurement points. However, the temperature rises of the chip and at measurement points 1 and 2 are higher at a high ambient temperature than those at a low ambient temperature. The optimal design 11# also shows improved heat transfer performance of the optimal design at an ambient temperature lower than 55 °C as

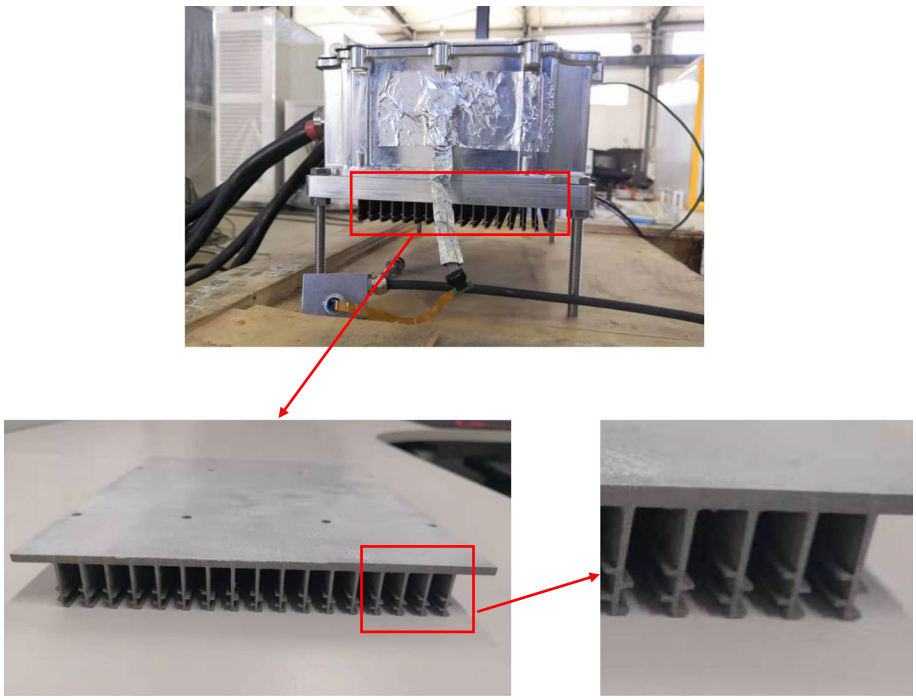

Fig. 12 Optimal design 11# for the heat sink with MCRFs

compared with the original heat sink, although the optimization work is done at an ambient temperature of 55 °C.

Here, we assumed that the equivalent temperatures at measurement points 1 and 2 equal the sum of the experimental data at an ambient temperature of 18 °C and the difference value between the CFD predicted data at the two ambient temperatures in experimental tests. The calculated equivalent temperature rises at the measurement point 1 and points 2 for the optimal design 11#, and the experimental data for the original design at the same ambient temperature of 32 °C are listed in Table 7.

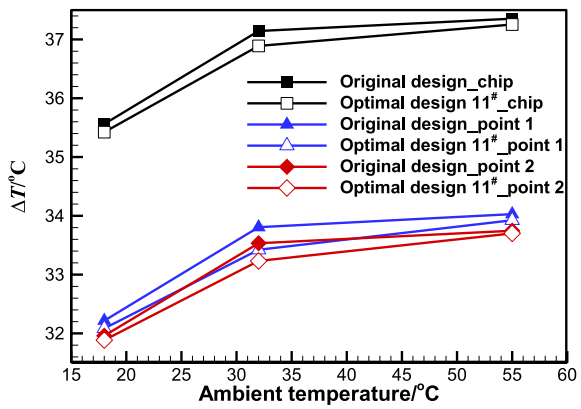

Fig. 13 Comparison of the temperature rise of the chip and at two measurement points under three ambient temperatures of 18 °C, 32 °C, and 55 °C

Table 7 The temperature rises at the measurement point 1 and 2 at an ambient temperature of 32°C

	Equivalent temperature rise for the original design (°C)	Experimental temperature rise for optimal design 11# (°C)
Point 1	34.93	35.01
Point 2	34.20	34.68

Although the equivalent temperature rises at either measurement point for the optimal design 11# are higher than that for the original design, the relative values are very close to the experimental data with different values of 0.08 °C and 0.48 °C. The comparison result indicates that the optimal design 11# with considerable heat transfer performance and a reduction in weight of 8.77% is feasible.

Conclusions

In the present work, multi-objective optimization has been performed to obtain the optimal design for the heat sink with multi-cross-ribbed-fins. As the current heat sink is equipped in the electrical drive truck motor controller, the minimizations of the temperature rise of the chip and the weight are pursued simultaneously. A mixed-level orthogonal design was employed to generate the sampling results by performing validated numerical simulations. The backpropagation neural network was trained to get the surrogate-based modeling between the objective functions and three design variables. The non-dominated sorting genetic algorithm II was utilized to determine the Pareto optimal solutions. The superiority of the optimal designs with multi-cross-ribbed-fins was testified by comparing the objective functions between the original design with smooth fins and the selected optimal design. Based on the result analysis and discussion, the following conclusions and future research directions can be drawn as follows:

1. As compared with the original smooth fin, the proposed multi-cross-ribbed-fin showed a larger area, heat transfer coefficient, and weight. Thus, the equivalent or even improved heat transfer performance but reducing weight for the heat sink can be achieved by reducing the number of the MCRFs.
2. The current multi-objective optimization methodology can competently reduce computational or experimental costs for the multi-cross-ribbed fin heat sink design with higher heat transfer performance and reduced weight. Compared with the original design, the chip's temperature has a maximum reduction of 7.63%, and a maximum reduction of 9.45% for the weight of the heat sink can be achieved. The recommended Pareto optimal designs for the heat sink with MCRFs were obtained. The design variables suggested corresponded to N_f=17~19, N_c=2–3, and h=2.13~2.59mm.
3. One of the Pareto optimal designs with an equivalent temperature rise of the chip and reduced weight was experimentally validated to illustrate the superiority of the current optimization methodology.
4. The final selection of which optimization solution still depends on the experience of the heat sink designers or the predilection in practice. It is recommended that a deci-

sion-making method should be coupled with the current optimization methodology in the future, for example, the technique for order preference by similarity to an ideal solution, to determine the final optimum solution from the Pareto solution set.

Abbreviations
ANN: Artificial neural network; BP: Backpropagation; CFD: Computational fluid dynamics; DC: Direct current; GA: Genetic algorithm; MCRF: Multi-cross-ribbed-fin; MOS: Metal-oxide-semiconductor; NSGA-II: Non-dominated sorting genetic algorithm II; PCB: Printed circuit board; RSM: Respond surface method; N_c: Number of the cross-ribs on one side of the MCRF; N_f: Number of the fins or the MCRFs; ΔT: Temperature rise relative to ambient temperature (°C); h: Height of the cross-rib (mm); m: Weight of the heat sink (kg).

Acknowledgements
The authors acknowledge the school of mechanical engineering at Tianjin University of Technology for providing lab facilities for performing simulations and Dr. Erxi Liu at the CATARC (Tianjin) Automotive Engineering Research Institute Co., Ltd., for the lab facilities for performing experiments.

Authors' contributions
ZC performed the simulation work and wrote the manuscript. CL performed the experimental work and analyzed the experimental data. TZ supervised the work and revised the manuscript. The authors read and approved the final manuscript.

Funding
The study is supported by the National Natural Foundation of China (Grant No. 51976139).

Availability of data and materials
The datasets analyzed during the current study are available from the corresponding author on reasonable request.

Declarations

Competing interests
The authors declare that they have no competing interests.

Author details
[1]Tianjin Key Laboratory for Advanced Mechatronic System Design and Intelligent Control, School of Mechanical Engineering, Tianjin University of Technology, Tianjin 300384, China. [2]National Demonstration Center for Experimental Mechanical and Electrical Engineering Education, Tianjin University of Technology, Tianjin 300384, China.

Received: 18 November 2021 Accepted: 2 March 2022
Published online: 16 March 2022

References
1. Chen HT, Lai ST, Haung LY (2013) Investigation of heat transfer characteristics in a plate-fin heat sink. Appl Therm Eng 50(1):352–360
2. Hong FJ, Cheng P (2009) Three dimensional numerical analyses and optimization of offset strip-fin microchannel heat sinks. Int Commun Heat Mass Transfer 36(7):651–656
3. Chai L, Xia GD, Zhou MZ, Li J, Qi JZ (2013) Optimum thermal design of interrupted microchannel heat sink with rectangular ribs in the transverse microchambers. Appl Therm Eng 51(1-2):880–889
4. Feng SS, Shi M, Yan HB, Sun SYM, Li FC, Lu TJ (2018) Natural convection in a cross-fin heat sink. Appl Therm Eng 132:30–37
5. Zhang K, Li MJ, Wang FL, He YL (2020) Experimental and numerical investigation of natural convection heat transfer of W-type fin arrays. Int J Heat Mass Transfer 152:119315
6. Nilpueng K, Ahn HS, Jerng DW, Wongwises S (2019) Heat transfer and flow characteristics of sinusoidal wavy plate fin heat sink with and without crosscut flow control. Int J Heat Mass Transfer 137:565–572
7. Zhou F, Catton I (2011) Numerical evaluation of flow and heat transfer in plate-pin fin heat sinks with various pin cross-sections. Numer Heat Transfer, Part A 60(2):107–128
8. Al-damook A, Alkasmoul F (2018) Heat transfer and airflow characteristics enhancement of compact plate-pin fins heat sinks – a review. Propul Power Res 7(2):138–146
9. Ahmed HE (2016) Optimization of thermal design of ribbed flat-plate fin heat sink. Appl Therm Eng 102:1422–1432
10. Wong KC, Indran S (2013) Impingement heat transfer of a plate fin heat sink with fillet profile. Int J Heat Mass Transfer 65:1–9
11. Hussain AA, Freegah B, Khalaf BS, Towsyfyan H (2019) Numerical investigation of heat transfer enhancement in plate-fin heat sinks: effect of flow direction and fillet profile. Case Stud Therm Eng 13:100388
12. Freegah B, Hussain AA, Falih AH, Towsyfyan H (2020) CFD analysis of heat transfer enhancement in plate-fin heat sinks with fillet profile: investigation of new designs. Therm Sci Eng Prog 17:100458

13. Singh P, Patil AK (2015) Experimental investigation of heat transfer enhancement through embossed fin heat sink under natural convection. Exp Therm Fluid Sci 61:24–33
14. Gupta A, Kumar M, Patil AK (2019) Enhanced heat transfer in plate fin heat sink with dimples and protrusions. Heat Mass Transfer 55:2247–2260
15. Tariq A, Aktaf K, Ahmad SW, Hussain G, Ratlamwala TAH (2021) Comparative numerical and experimental analysis of thermal and hydraulic performance of improved plate fin heat sinks. Appl Therm Eng 182:115949
16. Khudhur DS, Al-Zuhairy RC, Kassim MS (2022) Thermal analysis of heat transfer with different fin geometry through straight plate-fin heat sinks. Int J Therm Sci 174:107443
17. Li HY, Chen KY (2007) Thermal performance of plate-fin heat sinks under confined impinging jet conditions. Int J Heat Mass Transfer 50(9-10):1963–1970
18. Osorio JD, Rivera-Alvarez A, Ordonez JC (2017) Shape optimization of thin flat plate fins with geometries defined by linear piecewise functions. Appl Therm Eng 112:572–584
19. Kim DK, Jung J, Kim SJ (2010) Thermal optimization of plate-fin heat sinks with variable fin thickness. Int J Heat Mass Transfer 53(25-26):5988–5995
20. Tullius JF, Tullius TK, Bayazitoglu Y (2012) Optimization of short micro pin fins in minichannels. Int J Heat Mass Transfer 55(15-16):3921–3932
21. Webb RL (1981) Performance evaluation criteria for use of enhanced heat transfer surfaces in heat exchanger design. Int J Heat Mass Transfer 24(4):715–726
22. Yun JY, Lee KS (2000) Influence of design parameters on the heat transfer and flow friction characteristics of the heat exchanger with slit fins. Int J Heat Mass Transfer 43(14):2529–2539
23. Kulkarni K, Afzal A, Kim KY (2016) Multi-objective optimization of a double-layered microchannel heat sink with temperature-dependent fluid properties. Appl Therm Eng 99:262–272
24. Ge Y, Wang SC, Liu ZC, Liu W (2019) Optimal shape design of a minichannel heat sink applying multi-objective optimization algorithm and three-dimensional numerical method. Appl Therm Eng 148:120–128
25. Han HZ, Yu RT, Li BX, Zhang YN (2019) Multi-objective optimization of corrugated tube inserted with multi-channel twisted tape using RSM and NSGA-II. Appl Therm Eng 159:113731
26. Elsayed K, Lacor C (2011) Modeling, analysis and optimization of aircyclones using artificial neural network, response surface methodology and CFD simulation approaches. Powder Technol 212(1):115–133
27. Rao RV (2016) Design optimization of a plate fin heat sink using TLBO and ETLBO algorithms. In: Teaching Learning Based Optimization Algorithm. Springer, Cham
28. Lampio K, Karvinen (2017) Optimization of convectively cooled heat sinks. Microelectron Reliab 79:473–479
29. Mohammadpour J, Salehi F, Sheikholeslami M, Masoudi M, Lee A (2021) Optimization of nanofluid heat transfer in a microchannel heat sink with multiple synthetic jets based on CFD-DPM and MLA. Int J Therm Sci 167:107008
30. Damavandi MD, Forouzanmehr M, Safikhani H (2017) Modeling and Pareto based multi-objective optimization of wavy fin-and-elliptical tube heat exchangers using CFD and NSGA-II algorithm. Appl Therm Eng 111:325–339
31. Hojjat M (2020) Nanofluids as coolant in a shell and tube heat exchanger: ANN modeling and multi-objective optimization. Appl Math Comput 365:124710
32. Yildizeli A, Cadirci S (2020) Multi objective optimization of a micro-channel heat sink through genertic algorithm. Int J Heat Mass Transfer 146:118847
33. Shin HH, Yun S, Park MH, Jang DS, Kim Y (2022) Optimization of semi-interlocking heat sinks for hotspot thermal management using multi-objective genetic algorithm. Int J Heat Mass Transfer 183:122170
34. Ge Y, Lin YS, Yuan WZ, Chen JC, Huang SM (2022) Multi-objective optimization of a mini-channel heat sink with non-uniform fins using genetic algorithm in coupling with CFD methods. App Therm Eng 207:118127
35. Rahman AA, Zhang XQ (2018) Prediction of oscillatory heat transfer coefficient for a thermoacoustic heat exchanger through artificial neural network technique. Int J Heat Mass Transfer 124:1088–1096
36. Deb K, Pratap A, Agarwal S, Meyarivan T (2002) A fast and elitist multiobjective genetic algorithm: NSGA-II. IEEE Trans Evol Comput 6(2):182–197

Publisher's Note